

# Study of Multiple Coronal Mass Ejections at Solar Minimum Conditions

A. Bemporad · F.P. Zuccarello · C. Jacobs · M. Mierla ·  
S. Poedts

Received: 4 November 2011 / Accepted: 9 April 2012 / Published online: 7 June 2012  
© Springer Science+Business Media B.V. 2012

**Abstract** The aim of this work is to provide a physical explanation for the genesis of multiple coronal mass ejections (CMEs) in an asymmetric coronal field configuration. We analyze STEREO observations of a multiple eruption and compare the results from the data analysis with predictions provided by magnetohydrodynamic (MHD) simulations. To this end, the multiple CMEs (MCMEs) observed on 21–22 September 2009 were selected. Both eruptions originated from the same source region and showed approximately the same latitudinal deflection, by more than 15 degrees, toward the heliospheric current sheet (HCS) during their propagation in the COR1 field of view. Numerical MHD simulations of the MCMEs have been performed, starting from an asymmetric coronal field configuration that mimics the potential field source surface extrapolation for 21 September 2009. The results demonstrate that, by shearing the footpoints at the base of the southern arcade, we were able to reproduce the observed dynamics of the MCMEs. Both CMEs are deflected toward the HCS due to an

---

The Sun 360

Guest Editors: Bernhard Fleck, Bernd Heber, and Angelos Vourlidis

A. Bemporad (✉)

INAF, Osservatorio Astrofisico di Torino, Pino Torinese (TO), Italy  
e-mail: [bemporad@oato.inaf.it](mailto:bemporad@oato.inaf.it)

F.P. Zuccarello · C. Jacobs · S. Poedts

Centre for Plasma-Astrophysics, Department of Mathematics, KU Leuven, Leuven, Belgium

F.P. Zuccarello

e-mail: [Francesco.Zuccarello@wis.kuleuven.be](mailto:Francesco.Zuccarello@wis.kuleuven.be)

C. Jacobs

e-mail: [Carla.Jacobs@wis.kuleuven.be](mailto:Carla.Jacobs@wis.kuleuven.be)

F.P. Zuccarello

INAF, Osservatorio Astrofisico di Catania, Catania, Italy

M. Mierla

Institute of Geodynamics of the Romanian Academy, Bucharest, Romania

M. Mierla

Royal Observatory of Belgium, Brussels, Belgium

imbalance in the magnetic pressure and tension forces; the global field strength turns out to be a crucial parameter in order to release two subsequent eruptions, and hence to reproduce the observed evolution.

**Keywords** Coronal mass ejections, CMEs · Magnetic fields, corona · Simulations, MHD

## 1. Introduction

Coronal mass ejections (CMEs) are the most spectacular form of solar magnetic activity; during a typical CME  $10^{14} - 10^{16}$  g of plasma are suddenly ejected toward the interplanetary medium with velocities on the order of  $100 - 1000 \text{ km s}^{-1}$ . CMEs, solar flares, and filament eruptions are often associated, although their exact causal relationship is not yet well known. At times, CMEs occur in close succession: multiple coronal mass ejections (MCMEs) have been reported, for instance, by Burlaga, Plunkett, and St. Cyr (2002), Wang, Ye, and Wang (2003), Farrugia and Berdichevsky (2004), and Lugaz *et al.* (2008). Their possible interaction during propagation into interplanetary space is thought to be an important cause of geoeffective storms, large solar energetic particle (SEP) events, and intense type II radio bursts. Moreover, it has been suggested that MCMEs could be associated with multiple type II radio bursts (*e.g.*, Raymond *et al.*, 2000). The interaction of two successive CMEs and the resulting magnetic clouds has been investigated with numerical simulations (see, *e.g.*, Gonzalez-Esparza, Santillan, and Ferrer, 2004; Xiong, Zheng, and Wang, 2009; Shen *et al.*, 2011), focusing in particular on the problem of their geoeffectiveness. Collisions between two MCMEs may occur in the low corona, appearing as CME “cannibalism” (Gopalswamy *et al.*, 2001) where the faster ejection “swallows” the slower, preceding one. MCMEs are often associated with successive solar flares (see, *e.g.*, Liu *et al.*, 2009).

The MCMEs discussed in this work are neither sympathetic CMEs (SCMEs; *e.g.*, Simnett and Hudson, 1997; Moon *et al.*, 2003) nor homologous CMEs (HCMEs; *e.g.*, Zhang and Wang, 2002). SCMEs consist of a pair of consecutive CMEs originating from different active regions; the idea of “sympathetic” events historically alludes to flares occurring in close succession in time and involving different active regions, likely connected with each other by a cause–effect relationship. Hence, MCMEs are different from SCMEs, because they may originate from different active regions (like SCMEs) in close succession in time (as SCMEs), “sufficiently close” to allow interactions between the resulting interplanetary CMEs, but “not close enough” (for instance, with respect to the time required for the propagation of a wave over the Sun’s atmosphere or for coronal field diffusion) to allow the possibility of a direct cause–effect relationship (as occurs for SCMEs). Sympathetic filament eruptions and CMEs have been recently reported (Jiang *et al.*, 2011) and modeled (Török *et al.*, 2011).

HCMEs are more frequently reported than SCMEs, and their definition was originally clarified by Zhang and Wang (2002): two CMEs were considered to be HCMEs if both events i) were associated with homologous flares (Woodgate *et al.*, 1984), ii) had similar post-flare EUV dimmings, and iii) had a similar coronagraphic appearance. Because CMEs can occur without an associated (detectable) flare, the definition of HCMEs proposed by Zhang and Wang (2002) can be generalized simply by removing the first requirement. HCMEs occur within the same active region with almost the same background magnetic field, and so have similar shapes. However, SCMEs usually occur in different active regions connected by interconnecting magnetic loops, so in general SCMEs have different shapes, even if the concept of “sympathetic homologous CMEs” has been proposed (Cheng *et al.*,

2005). In fact, because flares are much more localized phenomena with respect to the larger scale CMEs, “it is plausible that two CMEs with associated flares at different locations could resemble each other in appearance and hence are classified to be HCMEs” (Cheng, Fang, and Chen, 2006). The occurrence of HCMEs was recently simulated, for instance, by Soenen *et al.* (2009), while Lugaz *et al.* (2007) focused on the mutual interaction between HCMEs during their propagation into interplanetary space.

In this work we focus on the occurrence of two MCMEs, *i.e.*, two successive eruptions which are neither SCMEs nor HCMEs. The study of MCMEs provides an interesting opportunity to test the efficiency of different physical candidate processes for the destabilization of CMEs and also to understand the large-scale reorganization of the coronal magnetic field during the events and how it affects the magnetic topology and stability of other magnetic structures. Both events reported here were observed with data acquired by the *Solar Terrestrial Relations Observatory* (STEREO; Kaiser *et al.*, 2008), and their three-dimensional (3D) trajectories were reconstructed. The first event was recently analyzed by Zuccarello *et al.* (2012, hereafter paper I), who focused on the observed latitudinal deflection. In this work we focus on the similarity between this first event and a second one, observed approximately seven hours later. In Section 2 we describe the two multiple events and the results from STEREO data analysis, in Section 3 we describe the numerical simulations we performed, and in Section 4 we summarize and discuss our results.

## 2. Observations

The two CMEs analyzed in this work occurred on 21–22 September 2009: at this time the angle between the STEREO spacecraft was about 116 degrees. Figure 1 shows a sequence of white light images acquired by the COR1 coronagraphs (Thompson *et al.*, 2003) onboard STEREO A and B (hereafter COR1-A and COR1-B, respectively). No flares were associated with these two eruptions. In order to enhance the visibility of both events, COR1 coronagraphic images are shown as running differences, so that white (black) color corresponds to an increase (decrease) of white light emission with respect to the previous frame, hence showing increases of local electron density. The time delay between two subsequent COR1 frames is five minutes. The visibility of the transient phenomena has been further enhanced first by thresholding running difference images and second by applying an image filtering process. In particular, the noise in the difference images has been reduced by applying a filter based on wavelet transforms, *i.e.*, by computing the discrete wavelet transform of each image, by discarding the wavelet coefficients smaller than a certain threshold, and then by computing again the inverse wavelet transform on the filtered coefficients in order to return the result. This analysis has been performed by employing the Coiflet family of wavelet functions.

Resulting images (Figure 1) show that on 21 September 2009 a first CME (left panels) was observed above the west (east) limb by STEREO B (STEREO A, respectively). This event (hereafter CME1) was better observed by COR1-B, where it shows a classical three-part structure; it was much more diffuse in the COR1-A images and the three-part components were not clearly observed compared with COR1-B images. As we described in paper I, the reason is that the CME1 core propagates at an approximate longitude of  $15^\circ\text{W}$  (as seen from the Earth), and thus along a plane which is  $\sim 19^\circ$  ( $\sim 44^\circ$ ) away from the COR1-B (COR1-A) plane of the sky (POS). The CME1 also underwent a strong latitudinal deflection during its propagation: the event was associated with a small prominence eruption that left the Sun from a latitude of  $34.3^\circ\text{S}$ , propagated northward, and finally resulted in

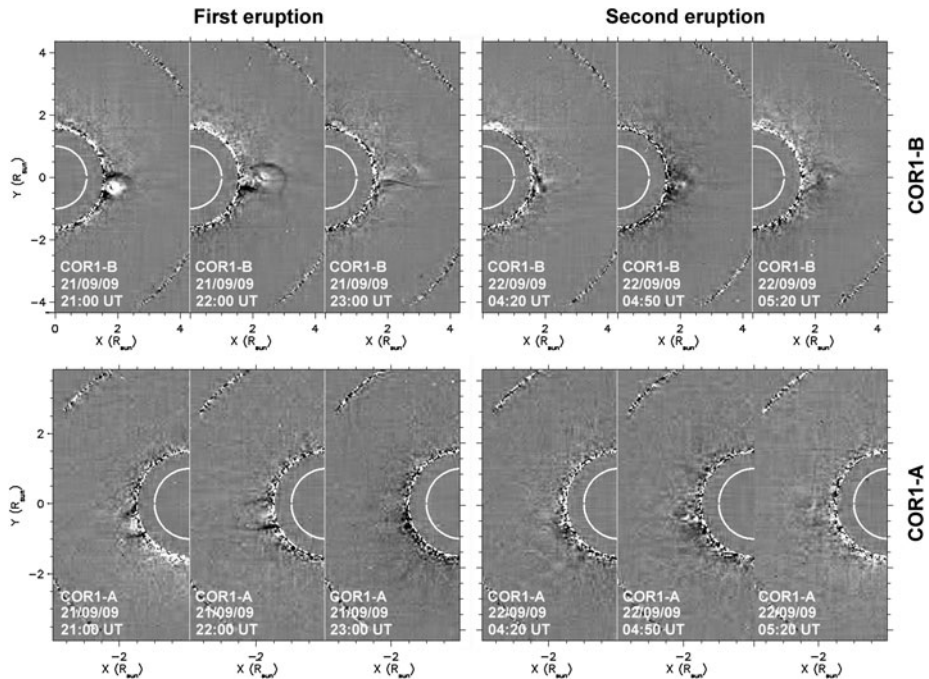


**Figure 1** The first (left) and second (right) eruptions as seen by the COR1 coronagraph onboard the STEREO B (top) and A (bottom) spacecraft. Images shown here are running differences filtered with wavelet transform in order to reduce the noise level (see text).

a CME propagating along the equatorial plane (see paper I for more details on the dynamics of this event). The reason for this deflection has been analyzed with magnetohydrodynamic (MHD) simulations in paper I. The results show that the CME1 was deflected toward the current sheet of the larger northern helmet streamer due to an imbalance in the magnetic pressure and tension forces and finally was absorbed into the streamer.

Interestingly, approximately eight hours later a second eruption (hereafter CME2) occurred: this is shown in Figure 1, right panels. CME2 is fainter than CME1, in both COR1-A and -B images, but follows approximately the same trajectory as CME1. The reason for this smaller white light brightness is probably related to the fact that CME1 was associated with a small prominence eruption (described in paper I), while no chromospheric material is seen to erupt during the CME2 occurrence. Hence, CME2 is likely associated with the propagation of lower density plasma with respect to CME1, in particular making the CME2 core fainter than the CME1 core. In the following hours both events propagate in the outer corona, as is better shown by images acquired with the COR2 instrument (Figure 2). The sequence of the COR2 images shows that both events enter in the telescope field of view (FOV) from the same coronal region and that, after the latitudinal deflection in the COR1 FOV described above, they propagate almost along a straight trajectory close to the equatorial plane.

To show the strong similarity between the CME1 and CME2 trajectories, we integrate the COR1 running difference images over different latitude or altitude intervals, in order to produce altitude versus time (the so called “*J*-maps”) and polar angle *versus* time maps, respectively (where the polar angle PA is measured from solar North counterclockwise). To this end, running difference images have been first converted pixel by pixel to polar coordi-

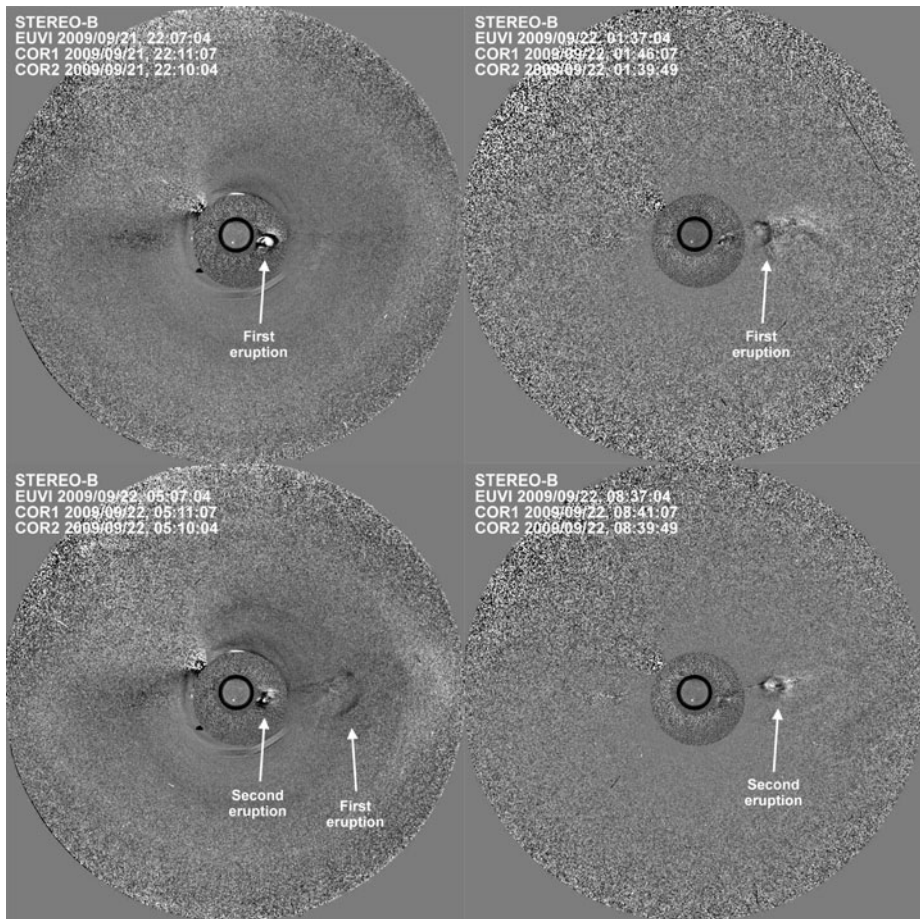


**Figure 2** The first and second eruptions as seen by the COR1 and COR2 coronagraphs and the EUVI telescope onboard STEREO B; UT times are provided in each panel. Images shown here are running differences: typical cadences during the above observational period were  $\approx 5$  minutes and  $\approx 15$  minutes for COR1 and COR2, respectively.

nates. Then, polar images have been integrated frame by frame over the polar angle intervals between  $PA = 85^\circ - 105^\circ$  (*i.e.*, between  $5^\circ\text{NE} - 15^\circ\text{SE}$  in projected COR1-A latitudes), and  $PA = 250^\circ - 270^\circ$  (*i.e.*,  $20^\circ\text{SW} - 0^\circ\text{W}$  in projected COR1-B latitudes), and over the altitude intervals between  $1.61 - 3.59$  solar radii for COR1-A, and  $1.63 - 3.97$  solar radii for COR1-B. By stacking the arrays computed with the preceding integrations in subsequent order as a function of time, we obtained the maps shown in Figure 3.

The altitude *versus* time maps (“ht-plot”, top panels) show that CME1 and CME2 had very similar acceleration profiles. Both CMEs show no significant acceleration above the projected altitude of  $\sim 2 R_\odot$ , and they propagate above that altitude with constant projected velocities of  $141 \text{ km s}^{-1}$  and  $155 \text{ km s}^{-1}$  in the COR1-B “ht-plot” and with velocities of  $74 \text{ km s}^{-1}$  and  $137 \text{ km s}^{-1}$  in the COR1-A “ht-plot” for CME1 and CME2, respectively. By taking into account the CME1 longitude of  $15^\circ\text{W}$  (see paper I), these projected velocities correspond to deprojected velocities of  $141/\cos(19^\circ) \approx 149 \text{ km s}^{-1}$  in COR1-B and

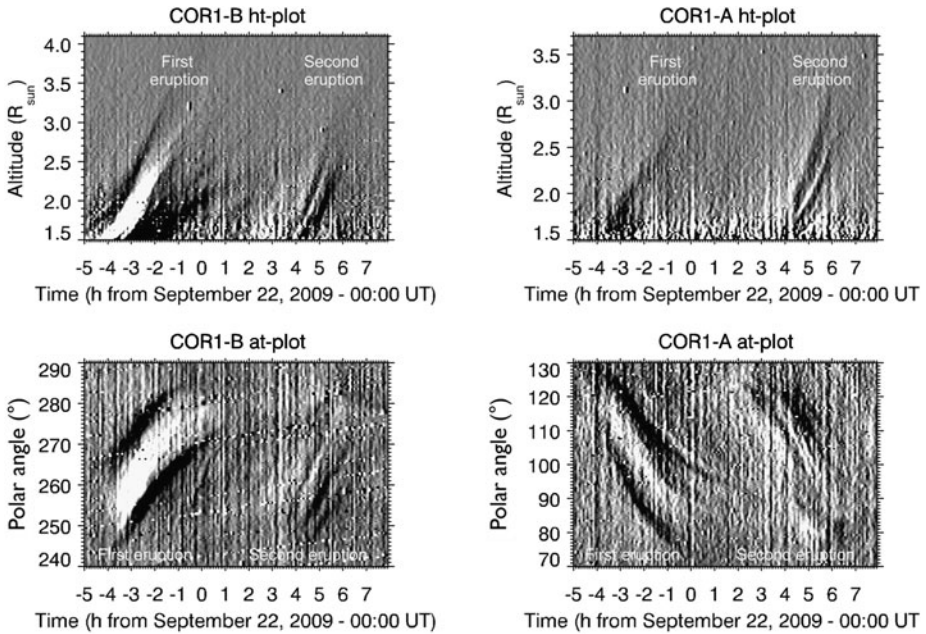


**Figure 3** Altitude *versus* time (top) and position angle *versus* time (bottom) evolution of both eruptions as seen from COR1-B (left) and COR1-A (right) coronagraphs.

$74/\cos(44^\circ) \simeq 103 \text{ km s}^{-1}$  in COR1-A. This small difference between the COR1-B and COR1-A velocities of CME1 are likely due to the fact that different parts of the same CME are sampled by the two instruments. The bottom panels in Figure 3 show that both CMEs also had very similar polar angle versus time maps (“at-plots”). In particular, both events appear in the COR1-B FOV at PA  $\simeq 250^\circ$  (*i.e.*,  $20^\circ$ SW in projected latitude), and then propagate northward toward the equator (PA =  $270^\circ$ ). At the same time, both events appear in the COR1-A FOV at PA  $\simeq 120^\circ$  (*i.e.*,  $30^\circ$ SE in projected latitude), and then propagate northward toward the equator (PA =  $90^\circ$ ).

In order to clarify how different geometries in the two eruptions implied differences in the “ht-plot” and “at-plot” of Figure 3, both events have been reconstructed with the Forward Modeling (FM) technique (Thernisien, Vourlidas, and Howard, 2009). For the FM technique we employed the *scraytrace* programs, freely distributed within the SolarSoftWare (SSW) package.<sup>1</sup> This model uses an empirically defined model of a flux rope, the graduated cylindrical shell (GCS), consisting of a tubular section attached to two cones that correspond to the legs of the CME. The shape (reminiscent of a “hollow croissant” model) and orientation of this 3D surface are defined by six free parameters. By comparing model results with observations by visual inspection, we optimized the free parameters by trial and error. Reconstructions have been performed on the running difference frames, by selecting the times when the upper edge of both CMEs lie approximately at the same altitude in the COR1-B images.

Results from the FM reconstructions are shown in Figure 4: in particular, CME1 (CME2) was reconstructed on 21 September 20:50 UT (22 September 04:40 UT) by

<sup>1</sup>See, *e.g.*, <http://www.lmsal.com/solarsoft/>.

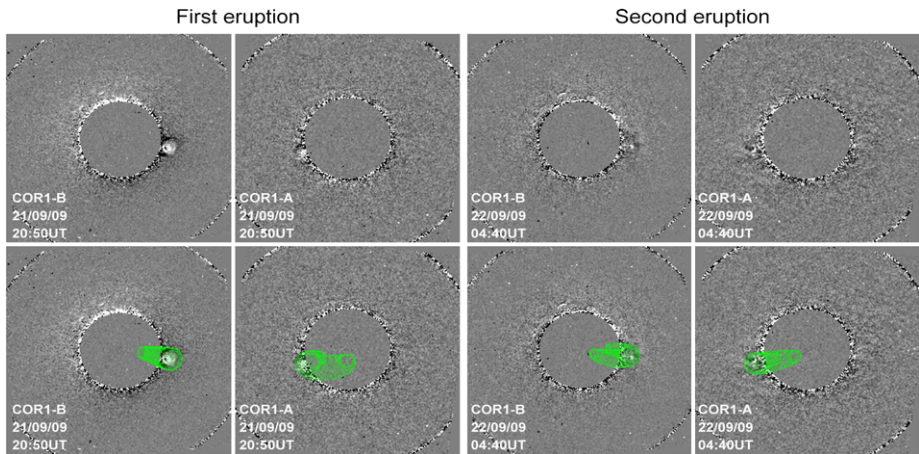


**Figure 4** Top: COR1 running difference images employed for the 3D reconstructions with FM technique. Bottom: superposition between the corresponding panels above and the 3D FM reconstructions (green wire grid) of CME1 (left) and CME2 (right).

centering the flux rope at the altitude  $r$ , latitude  $\theta$ , and longitude  $\phi$  of  $[r, \theta, \phi] = [2.50 R_{\odot}, 14.0^{\circ}\text{S}, 15.0^{\circ}\text{W}]$  ( $[2.5 R_{\odot}, 10.1^{\circ}\text{S}, 10.5^{\circ}\text{E}]$ ). Moreover, a difference of about  $11^{\circ}$  between the CME1 and CME2 flux rope tilt angles was required in order to better reproduce the observations. Both CMEs propagated toward the Earth, CME1  $\sim 15^{\circ}$  westward and CME2  $\sim 10^{\circ}$  eastward with respect to the Sun–Earth line, hence following very similar trajectories. Moreover, the above longitudes are consistent with the observational fact (also shown in Figure 2 and Figure 3) that CME1 is much brighter in COR1-B than in COR1-A images, while CME2 is slightly brighter in COR1-A than in COR1-B images. In fact, taking into account that the STEREO-B (STEREO-A) separation angle with the Earth was  $55.6^{\circ}$  ( $60.8^{\circ}$ ), the CME1 central longitude was closer to the COR1-B than to the COR1-A POS ( $\sim 19^{\circ}$  and  $\sim 44^{\circ}$  away from the COR1-B and -A POS, respectively), while the CME2 was closer to the COR1-A than to the COR1-B POS ( $\sim 19^{\circ}$  and  $\sim 45^{\circ}$  away from the COR1-A and -B POS, respectively).

The white light and EUV coronal evolutions during and after these two events are shown in Figure 5. The COR1-B images acquired before CME1 (top left), between CME1 and CME2 (top middle), and after CME2 (top right) have a very similar appearance. This shows that the intermediate corona is basically unaffected by these eruptions; only a progressive slow decrease of the total density around the eruption region can be observed, likely associated with the coronal plasma dragged by the two CMEs. Images from the *Solar and Heliospheric Observatory* (SOHO) *Extreme Ultraviolet Imaging Telescope* (EIT, Fe XII 195 filter) show that the lower EUV corona is also basically unaffected by these two CMEs; clear dimmings are neither visible after CME1 (bottom middle) nor after CME2 (bottom right) if compared with the pre-CME image (bottom left).

### 3. Simulations

In order to reproduce the key characteristics of the described events, we follow a similar approach as in previous works (Zuccarello *et al.*, 2009, 2012). The ideal MHD equations are solved numerically on a spherical, axisymmetric (2.5D) domain covering the region

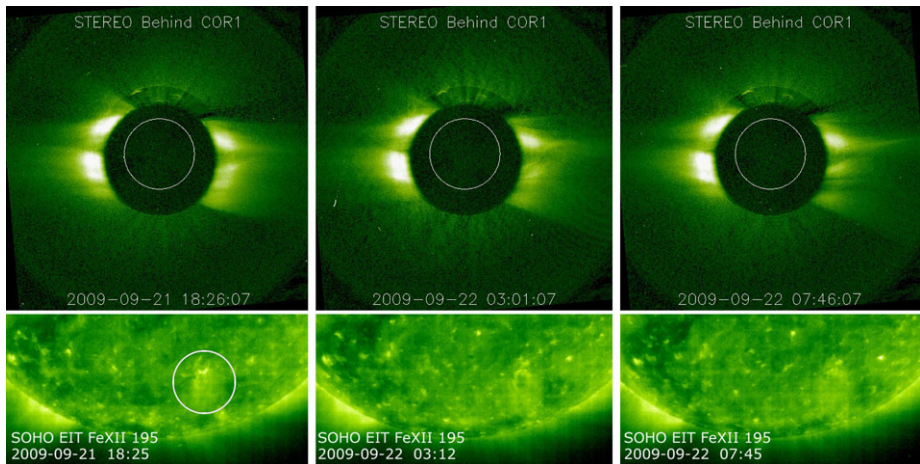


**Figure 5** Top: the white light corona as seen by COR1-B before CME1 (left), between CME1 and CME2 (middle), and after CME2 (right). Bottom: the EUV corona as seen by SOHO EIT (Fe XII filter) approximately at the same times as the above COR1 images. The white light circle surrounds the source region of the erupting prominence associated with CME1.

between the solar north and south poles, *i.e.*,  $(r, \vartheta) \in [1 R_{\odot}, 30 R_{\odot}] \times [0, \pi]$ . The domain is discretized by a non-equidistant grid with  $480 \times 201$  cells. All simulations are performed with a modified version of the Versatile Advection Code (VAC) (Tóth, 1996), using a two-step Runge–Kutta scheme in time, while for the spatial discretization we use a second-order finite volume scheme. To reproduce a bimodal solar wind structure, an additional volumetric heating/cooling term (Groth *et al.*, 2000; Manchester *et al.*, 2004) resembling the effect of radiative losses, thermal conduction, and other heating mechanisms is added to the energy equation.

The initial magnetic field configuration for the simulation as well as the boundary conditions have been discussed in paper I. In brief, our initial condition consists of a global dipole field with a strength of about 2.2 G at the poles to which, in the southern hemisphere, an extra antiparallel bipolar flux system with a maximum magnetic field strength of about 1 G is added, creating a multiple arcade structure. Therefore, the only difference from paper I is the strength of the global dipole; for the simulation discussed in this paper, it is 33 % stronger. As a result of the increased strength of the global dipole field, the configuration of the system differs with respect to paper I. Figure 6 shows the magnetic configuration of the system when the steady state is reached for both the paper I simulation (Figure 6, left panel) and the simulation presented here (Figure 6, right panel). As a result of the stronger ambient field, the pseudostreamer (Wang, Sheeley, and Rich, 2007) structure vanishes. Instead, the system consists of an overlying helmet streamer that connects the north and south hemispheres of the Sun and, within it, a triple arcade structure. The inner arcade has the opposite orientation of the overlying magnetic field, and as such a configuration favorable for magnetic breakout is obtained.

First, the configuration is relaxed in time until a stationary solution for the corona and solar wind is obtained. Next, similarly to the method of simulation discussed in paper I, localized, time-dependent shearing motions along the southernmost polarity inversion line are applied. The shear flow shows variation in both latitude and time and is applied for a period of 36 h. At  $t = 18$  h the maximum shear velocity is reached. As a consequence of

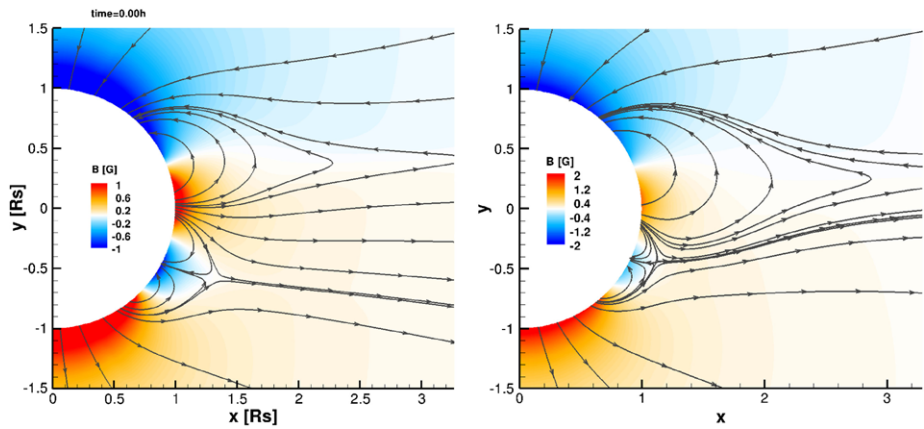


**Figure 6** Magnetic field distribution (color scale) and selected field lines for the stationary state of (left) the simulation of paper I and (right) the simulation of the present paper.

the applied shearing motions the magnetic pressure inside the southern arcade increases and the arcade starts to expand, eventually compressing the X-point above the central arcade. As a result, magnetic reconnection between the southern and the northern arcade sets in. This reconnection process transfers the flux of the southern arcade partially to the overlying helmet streamer and partially to the central arcade, eventually facilitating the expansion of the southern arcade. Meanwhile, as a consequence of the imbalance between the magnetic pressure and the magnetic tension, due to the shearing profile (see paper I), the flanks of the southern arcade pinch together, resulting in the formation of a flux rope (Figure 7, top left). About 17 h after the beginning of the shearing motions, because of the ongoing reconnection between the southern and northern arcade on one hand and reconnection below the flux rope on the other hand, the flux rope moves toward the equator and merges with the northern arcade that undergoes an expansion (Figure 7, top right).

In Zuccarello *et al.* (2009) the reconnection between the expanding central arcade and the overlying field detaches the helmet streamer, eventually resulting in a CME. In this simulation the magnetic field of the intruded flux rope has the same orientation as the closed field lines of the overlying helmet streamer; therefore, no reconnection between the flux rope field and the overlying field is observed for this event. As a result, the magnetic tension actually slows down the flux rope. However, the current associated with the flux rope is anti-parallel to the current of the northern arcade, resulting in an outward directed Lorentz force, which, in combination with the acceleration of the background solar wind leads to the ejection of the CME1 along the helmet streamer. At this point, the perturbed southern arcade is still subjected to shearing motions; thus, it rises again and reconnects with the magnetic field of the northern arcade, causing the growth of the central arcade. However, the strength of the azimuthal magnetic field built up in the southern arcade is weaker than during the first eruption since we are in the decaying phase of the shear profile. Therefore, the southern arcade does not expand, but is squeezed between the growing central arcade and the ambient field (Figure 7, bottom left). Due to this compression the plasma density increases in the southern flank of the streamer, and reconnection between the stretched ambient field and the enlarged central arcade results in a mass outflow along the magnetic field lines (Figure 7, bottom right). This plasma outflow eventually stretches the cusp of the northern arcade, which will be pinched off, leading to the formation of a second flux rope.

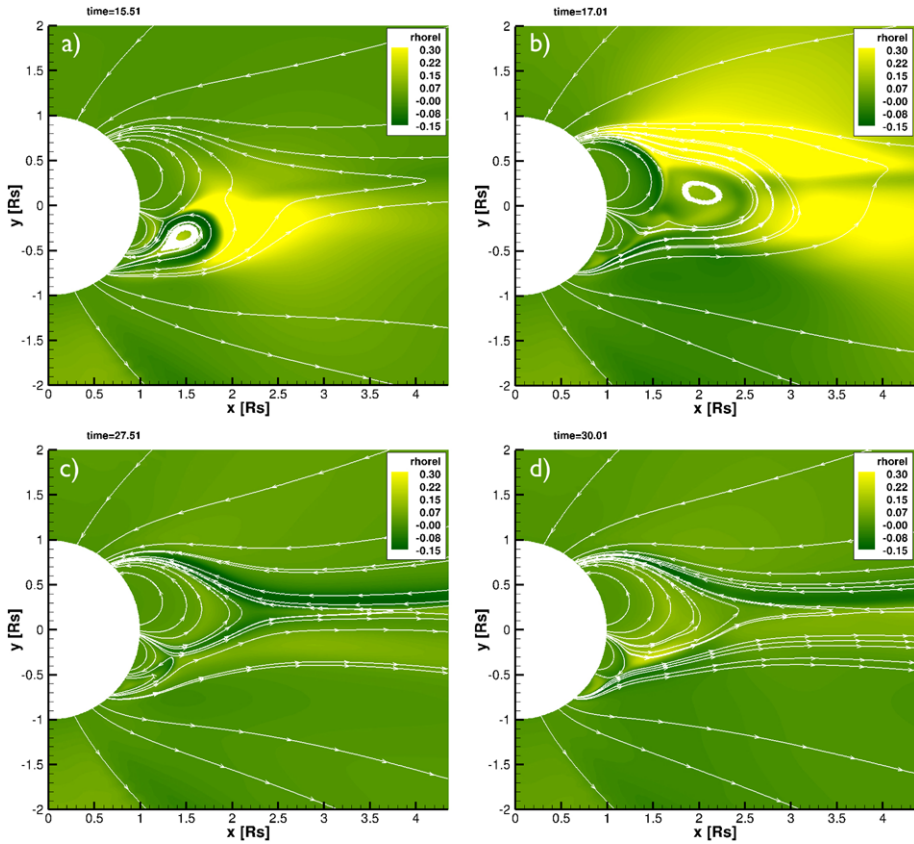


**Figure 7** Snapshots of the time evolution of the relative density, *i.e.*,  $(\rho(t) - \rho(t = 0))/\rho(t = 0)$  (color scale), and of selected field lines (white lines) during the formation of the flux rope associated with CME1 (a), the flux rope movement toward the equator (b), the following rising of the southern arcade (c), and the mass outflow associated with CME2 (d).

Figure 8 visualizes the density relative to the steady-state background solar wind density as both simulated CMEs are ploughing through the COR1 and COR2 FOVs at different instances in time: the first snapshot shows the propagation of the CME1, the second shows CME1 and the onset of CME2, while in the third snapshot both MCMEs are visible. Finally, in the fourth snapshot the CME2 is propagating through the numerical domain. A comparison between snapshot three and snapshot four clearly shows that CME1 is much wider than CME2. As discussed in the previous section, during their initial evolution, the MCMEs undergo a deflection toward the equator. To follow both the latitudinal and the radial evolution of the flux ropes during their expansion, we produced relative density  $J$ -maps in a similar fashion as was done for the observations. Figure 9 (left) shows the latitude *versus* time plot. The three-part structure of CME1 is evident: the leading bright edge is followed by the dark cavity and finally by the core of CME1. During the propagation the core of CME1 undergoes a latitudinal deflection of about  $20^\circ$ , eventually approaching the solar equator. The figure also shows an increase in the density around time 35 h, corresponding to the core of CME2. From the simulation one can deduce that the first flux rope is formed at an altitude of about  $1.35 R_\odot$  and about 17 h after the beginning of the shearing motions. Within one hour

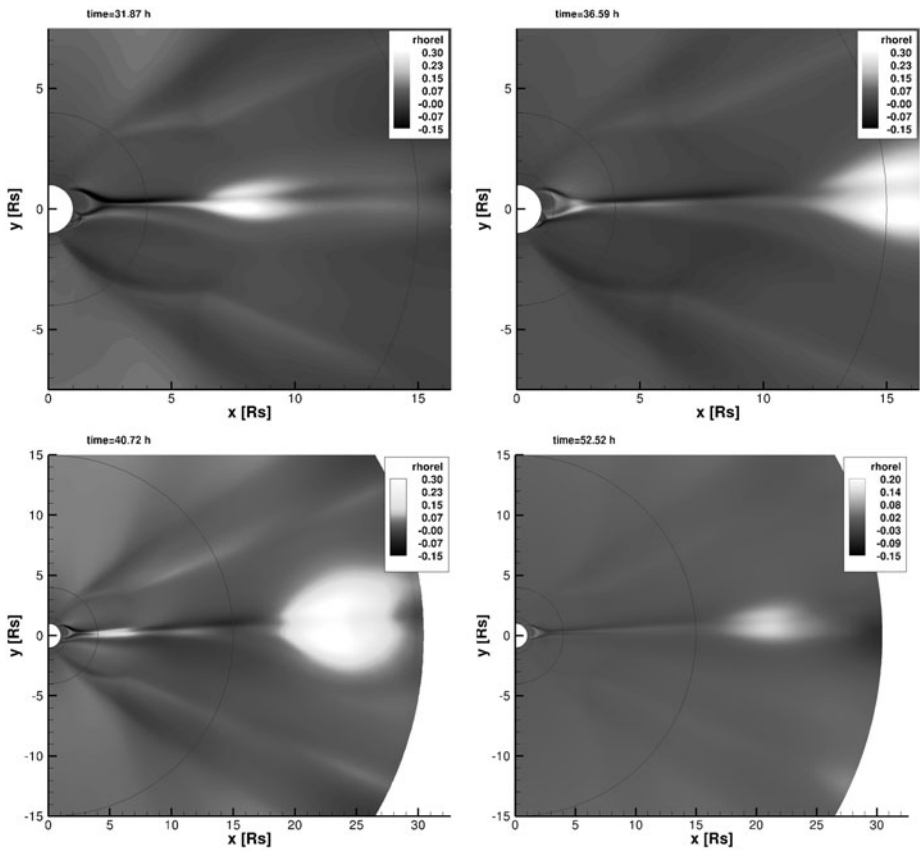


**Figure 8** Selected snapshots of the evolution of the relative density where both simulated CMEs are visible.

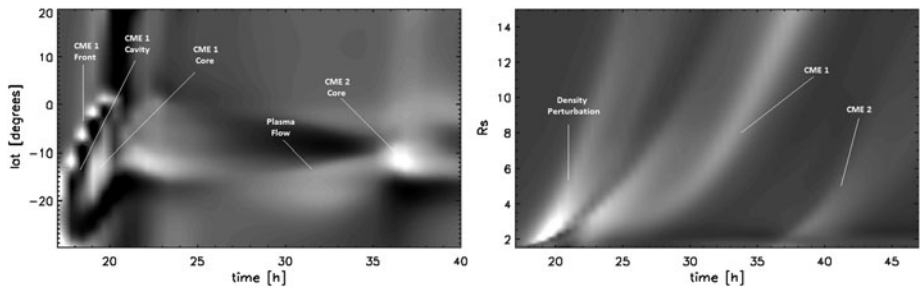


**Figure 9** Latitude versus time (left) and altitude versus time (*J*-maps, right) for the two CMEs.

it enters the COR1 FOV and after about five hrs it reaches the COR2 FOV, as illustrated in the right panel of Figure 9. After about 35 h the second flux rope also appears in the COR1 FOV.

#### 4. Discussion and Conclusions

In this work we focused on the occurrence of two multiple CMEs (MCMEs). In summary, observations acquired by the COR1 and COR2 coronagraphs onboard STEREO show that both eruptions have similar altitude versus time and latitude versus time profiles (Figure 3), propagate outwards approximately along the same path (Figure 4), and leave the same post-eruption coronal configuration both in white light and EUV images (Figure 5). This may give the impression that both eruptions are produced in a similar manner in the same coronal region, and hence that these are homologous CMEs. Nevertheless, these two events also have significant differences, as we concluded from white light and EUV observations. First, CME1 was associated with a prominence eruption, while this was not the case for CME2. This might also explain the difference in the white light brightness of these events. Second, the three-part structure of CME1 was already visible in white light in the early phases of the eruption (Figure 2, top left), while CME2 appeared initially more “unstructured” (Figure 2, bottom left) and a “front-like” feature formed only hours later (Figure 2, bottom right). As suggested by the 3D reconstructions performed with the FM technique, these different morphologies could be partly due to their different central longitude of propagation and to their different tilt angles, but also to the fact that, as mentioned, only the first event was associated with a prominence eruption.

In order to better understand these differences/similarities, 2.5D MHD numerical simulations have been performed, starting from an initial coronal magnetic field configuration that resembles (see paper I) the coronal field obtained from potential field source surface (PFSS) extrapolations. Our simulation suggests that the mechanisms at the origin of the two CMEs are different. In the simulation the first CME is formed as a result of the applied shearing motions along the polarity inversion line of the southern arcade, while the second CME is almost entirely the consequence of the rearrangement of the coronal field after the first eruption. This differs from the simulation by DeVore and Antiochos (2008), in which a sequence of successive HCMEs was initiated in the same source region via continuous shearing motions, *i.e.*, by the same initiation mechanism. By contrast, the MCMEs discussed above, although they originate from the same coronal source region, are the result of two different initiation mechanisms.

A comparison between the synthetic (Figure 9) and the observed (Figure 3)  $J$ -maps shows that CME2 is initiated four to five hours later with respect to the observed map. However, the simulation is able to reproduce both the latitudinal deflection and the radial evolution for both MCMEs. We believe that the discrepancy is due to the stronger than observed global magnetic field, whose magnetic tension will definitely slow down CME2. A comparison with the results of paper I shows how a relatively small change in the strength of the global dipole field can significantly influence the dynamics of the CMEs, leading us to conclude that the global field strength is a crucial parameter for reproducing the observed CME evolution. The strength of the global dipole field turns out to be a crucial factor for obtaining the second eruption. Although exactly the same driving mechanism was used in paper I, no secondary eruption was present in that simulation.

**Acknowledgements** The authors thank the anonymous referee for very useful comments. This research was funded by projects GOA-2009-009 (K.U.Leuven), G.0729.11 (FWO Vlaanderen), 3E090665 (FWO Vlaanderen), and C 90347 (ESA Prodex 9). The research leading to these results has received funding from the European Commission’s Seventh Framework Programme (FP7/2007-2013) under the grant agreement SWIFF (project n. 263340, [www.swiff.eu](http://www.swiff.eu)). For the simulations we used the infrastructure of the VSC – Flemish Supercomputer Center, funded by the Hercules foundation and the Flemish Government – department EWI. STEREO is a NASA project. Part of the work of MM was covered by the project TE 73/11.08.2010.

## References

- Burlaga, L.F., Plunkett, S.P., St. Cyr, O.C.: 2002, Successive CMEs and complex ejecta. *J. Geophys. Res.* **107**, 1266.
- Cheng, J.-X., Fang, C., Chen, P.-F., Ding, M.-D.: 2005, Two sympathetic homologous CMEs on 2002 May 22. *Chin. J. Astron. Astrophys.* **5**(3), 265–272.
- Cheng, J.X., Fang, C., Chen, P.F.: 2006, Two candidate homologous CMEs on 2002 May 22. *Adv. Space Res.* **38**, 470–474.
- DeVore, C.R., Antiochos, S.K.: 2008, Homologous confined filament eruptions via magnetic breakout. *Astrophys. J.* **680**, 740.
- Farrugia, C.J., Berdichevsky, D.: 2004, Evolutionary signatures in complex ejecta and their driven shocks. *Ann. Geophys.* **22**, 3679–3698.
- Gonzalez-Esparza, A., Santillan, A., Ferrer, J.: 2004, A numerical study of the interaction between two ejecta in the interplanetary medium: one- and two-dimensional hydrodynamic simulations. *Ann. Geophys.* **22**, 3741–3749.
- Gopalswamy, N., Yashiro, S., Kaiser, M.L., Howard, R.A., Bougeret, J.L.: 2001, Radio signatures of coronal mass ejection interaction: coronal mass ejection cannibalism? *Astrophys. J. Lett.* **548**, L91–L94.
- Groth, C.P.T., De Zeeuw, D.L., Gombosi, T.I., Powell, K.G.: 2000, Three-dimensional MHD simulation of coronal mass ejections. *J. Geophys. Res.* **105**, 25053–25078.
- Liu, C., Lee, J., Karlický, M., Prasad Choudhary, D., Deng, N., Wang, H.: 2009, Successive solar flares and coronal mass ejections on 2005 September 13 from NOAA AR 10808. *Astrophys. J.* **703**, 757–768.
- Jiang, Y., Yang, J., Hong, J., Bi, Y., Zheng, R.: 2011, Sympathetic filament eruptions connected by coronal dimmings. *Astrophys. J.* **738**, 179–186.
- Kaiser, M.L., Kucera, T.A., Davila, J.M., St. Cyr, O.C., Guhathakurta, M., Christian, E.: 2008, *Space Sci. Rev.* **136**, 5–16.
- Lugaz, N., Manchester, W.B. IV, Roussev, I.I., Tóth, G., Gombosi, T.I.: 2007, Numerical investigation of the homologous coronal mass ejection events from active region 9236. *Astrophys. J.* **659**, 788–800.
- Lugaz, N., Manchester, W.B. IV, Roussev, I.I., Gombosi, T.I.: 2008, Observational evidence of CMEs interacting in the inner heliosphere as inferred from MHD simulations. *J. Atmos. Solar-Terr. Phys.* **70**, 598–604.
- Manchester, W.B., Gombosi, T.I., Roussev, I., Ridley, A., De Zeeuw, D.L., Sokolov, I.V., Powell, K.G., Tóth, G.: 2004, Modeling a space weather event from the Sun to the Earth: CME generation and interplanetary propagation. *J. Geophys. Res.* **109**, A02107.
- Moon, Y.-J., Choe, G.S., Wang, H., Park, Y.D.: 2003, Sympathetic coronal mass ejections. *Astrophys. J.* **588**, 1176–1182.
- Raymond, J.C., Thompson, B.J., St. Cyr, O.C., Gopalswamy, N., Kahler, S., Kaiser, M., Lara, A., Ciaravella, A., Romoli, M., O’Neal, R.: 2000, SOHO and radio observations of a CME shock wave. *Geophys. Res. Lett.* **27**, 1439–1442.
- Shen, F., Feng, X.S., Wang, Y., Wu, S.T., Song, W.B., Guo, J.P., Zhou, Y.F.: 2011, Three-dimensional MHD simulation of two coronal mass ejections’ propagation and interaction using a successive magnetized plasma blobs model. *J. Geophys. Res.* **116**, A09103.
- Simnett, G.M., Hudson, H.S.: 1997, The evolution of a rapidly-expanding active region loop into a trans-equatorial coronal mass ejection, In: *Correlated Phenomena at the Sun, in the Heliosphere and in Geospace. 31st ESLAB Symposium SP-415*, ESA, Noordwijk, 437–441.
- Soenen, A., Zuccarello, F.P., Jacobs, C., Poedts, S., Keppens, R., van der Holst, B.: 2009, Numerical simulations of homologous coronal mass ejections in the solar wind. *Astron. Astrophys.* **501**, 1123–1130.
- Thernisien, A., Vourlidis, A., Howard, R.A.: 2009, Forward modeling of coronal mass ejections using STEREO/SECCHI data. *Solar Phys.* **256**(1–2), 111–130.
- Thompson, W.T., Davila, J.M., Fisher, R.R., et al.: 2003, COR1 inner coronagraph for STEREO-SECCHI. *Proc. SPIE* **4853**, 1–11.
- Tóth, G.: 1996, A general code for modeling MHD flows on parallel computers: versatile advection code. *Astrophys. Lett. Commun.* **34**, 245.
- Török, T., Panasenco, O., Titov, V.S., Mikić, Z., Reeves, K.K., Velli, M., Linker, J.A., De Toma, G.: 2011, A model for magnetically coupled sympathetic eruptions. *Astrophys. J. Lett.* **739**, L63.
- Xiong, M., Zheng, H., Wang, S.: 2009, Magnetohydrodynamic simulation of the interaction between two interplanetary magnetic clouds and its consequent geoeffectiveness: 2. Oblique collision. *J. Geophys. Res.* **114**, A11101.
- Wang, Y.-M., Sheeley, N.R. Jr., Rich, N.B.: 2007, Coronal pseudostreamers. *Astrophys. J.* **658**, 1340–1348.
- Wang, Y.M., Ye, P.Z., Wang, S.: 2003, Multiple magnetic clouds: Several examples during March–April 2001. *J. Geophys. Res.* **108**, 1370.

- Woodgate, B.E., Martres, M.-J., Smith, J.B. Jr., Strong, K.T., McCabe, M.K., Machado, M.E., Gaizauskas, V., Stewart, R.T., Sturrock, P.A.: 1984, Progress in the study of homologous flares on the Sun. II. *Adv. Space Res.* **4**, 11–17.
- Zhang, J., Wang, J.: 2002, Are homologous flare-coronal mass ejection events triggered by moving magnetic features? *Astrophys. J.* **566**, L117–L120.
- Zuccarello, F.P., Jacobs, C., Soenen, A., Poedts, S., van der Holst, B., Zuccarello, F.: 2009, Modelling the initiation of coronal mass ejections: magnetic flux emergence versus shearing motions. *Astron. Astrophys.* **507**, 441–452.
- Zuccarello, F.P., Bemporad, A., Jacobs, C., Mierla, M., Poedts, S., Zuccarello, F.: 2012, The role of streamers in the deflection of coronal mass ejections: comparison between STEREO 3D reconstructions and numerical simulations. *Astrophys. J.* **744**, 66.